ADVANCED ENERGY MATERIALS
www.advenergymat.de

Cation-Diffusion-Based Simultaneous Bulk and Surface Passivations for High Bandgap Inverted Perovskite Solar Cell Producing Record Fill Factor and Efficiency

Md Arafat Mahmud, Jianghui Zheng, Shi Tang, Guoliang Wang, Jueming Bing, Anh Dinh Bui, Jiangtao Qu, Limei Yang, Chwenhaw Liao, Hongjun Chen, Stephen P. Bremner, Hieu T. Nguyen, Julie Cairney, and Anita W. Y. Ho-Baillie**

High bandgap perovskite solar cells are integral to perovskite-based multi-junction tandem solar cells with efficiency potentials over 40%. However, at present, high bandgap perovskite devices underperform compared to their mid bandgap counterparts in terms of voltage outputs and fill factors resulting in lower than ideal efficiencies. Here, the low fill factor aspect of high bandgap perovskite is addressed by developing a cation-diffusion-based double-sided interface passivation scheme that simultaneously provides bulk passivation for a 1.75 eV perovskite cell that is also compatible with a p-i-n cell architecture. The champion cell achieves a record fill factor of 86.5% and a power conversion efficiency of 20.2%. Results of ionic distribution profiling, Fourier transform infrared spectroscopy, and X-ray diffraction crystallography reveal evidence of cation diffusion from the surface perovskite passivation layer into bulk. The diffused cations reduce Shockley–Read–Hall recombination in the perovskite bulk and at the surfaces with the latter being more dominant as confirmed by light-intensity dependent and temperature-dependent open-circuit voltage measurements as well as thermal admittance spectroscopy. This concurrent bulk and surface passivation scheme renders record fill factor and efficiency in the double-side passivated cells. This provides new insights for future passivation strategies based on ionic diffusion of functionalized materials.

1. Introduction

Metal halide perovskite solar cell is the fastest-growing photovoltaic technology in terms of efficiency improvement. The best laboratory 1.53 eV cell efficiency has reached 25.7% from 3.8% in just over 10 years.[1] As a wide range (1.2 to 2.3 eV) of bandgap is realisable for perovskites by tuning their composition in precursor preparation, perovskites are suitable for low-cost, solution-processable multijunction tandem solar cells, having an efficiency potential over 40%.[2] High bandgap (1.7 to 2.0 eV) perovskite cells are integral to such tandems, but current demonstrations suffer from high voltage deficit: W_{oc} (= $E_{th/q} - V_{oc}$) where E_{th} is the absorption edge, loosely used as "bandgap", and q is elementary charge[3] compared to their low mid-bandgap (1.5 to 1.6 eV) counterparts producing lower voltage outputs, lower fill factors (FF) in high bandgap devices (Figure S1, Supporting Information) indicating room for improving bulk

M. A. Mahmud, J. Zheng, S. Tang, G. Wang, J. Bing, C. Liao, H. Chen, A. W. Y. Ho-Baillie
School of Physics
The University of Sydney
Sydney, NSW 2006, Australia
E-mail: md.mahmud@sydney.edu.au; anita.ho-baillie@sydney.edu.au

M. A. Mahmud, J. Zheng, S. Tang, G. Wang, J. Bing, C. Liao, H. Chen, A. W. Y. Ho-Baillie
The University of Sydney Nano Institute (Sydney Nano)
The University of Sydney
Sydney, NSW 2006, Australia

The ORCID identification number(s) for the author(s) of this article can be found under https://doi.org/10.1002/aenm.202201672.

DOI: 10.1002/aenm.202201672

J. Zheng, S. P. Bremner, A. W. Y. Ho-Baillie
Australian Centre for Advanced Photovoltaics (ACAP)
School of Photovoltaic and Renewable Energy Engineering
University of New South Wales
Sydney 2052, Australia

J. Zheng
Sustainable Energy Research Centre
School of Engineering
Macquarie University
Sydney, NSW 2109, Australia

A. D. Bui, H. T. Nguyen
School of Engineering
The Australian National University
ACT 2601, Australia

J. Qu, L. Yang, J. Cairney
Australian Centre for Microscopy and Microanalysis (ACMM)
The University of Sydney
Sydney, NSW 2006, Australia

and interface quality,[4] reducing their susceptibilities to carrier recombination.

A number of recent studies have focussed on bulk[5] and/or surface passivation[6] of high bandgap perovskite films to reduce their trap-assisted recombination. A major limitation in the demonstrated passivation strategies is that the passivation effect is confined to either bulk or only at one perovskite/charge-transport-layer interface. Another limitation is the type of perovskite devices that have benefited from successful passivation strategies. For example, double-sided interface passivation has been shown to be successful for mid bandgap perovskite cells which are predominantly n–i–p devices[7] where the n-type layers are fabricated first and p-type layers are fabricated last. Since p–i–n devices have less optically absorptive transport layers on the sun-facing side, they can achieve higher efficiency potentials than n–i–p ones for tandem application.[8] However, there is only one report for "inverted" p–i–n mid-bandgap (≈1.55 eV) perovskite device with double-sided interface passivation[9] warranting more research on p–i–n device in suppressing nonradiative recombination within the bulk and at both perovskite/charge-transport-layer interfaces. Double-sided interface passivation is yet to be demonstrated for high-bandgap perovskites. In the work by Degani et al.[9] the surface passivating layers consist of large PEAI-based cations (in the form of 2-phenylethylammonium iodide (PEAI), 4-chloro-phenylethylammonium iodide (Cl-PEAI) or 4-fluoro-phenylethylammonium iodide (F-PEAI)). The layers were fabricated by dissolving PEAI-based cations in dimethylformamide (DMF) or in a mixture of chlorobenzene (CB) with isopropyl alcohol (IPA). The former (PEAI in DMF) would be deposited on the hole-transport-layer HTL before the fabrication of the perovskite absorber while the latter (PEAI in CB-IPA) will be deposited on the perovskite absorber prior to electron-transport-layer (ETL) fabrication. This method is suitable for HTLs that are hydrophobic but not so for self-assembly monolayer (SAM)-based HTLs that are recently becoming popular for the state-of-the-art high efficiency perovskite solar cells.[8] Controlling the concentration of passivation cations in solvent such as CB can also be difficult due to the low solubility of halide salts. This may result in process variation, adversely affecting device reproducibility.

In this work, we develop a double-sided surface passivation that also provides bulk passivation for perovskite cells at the same time. This method has been demonstrated to be successful for p–i–n perovskite cells. This is the first time such passivation scheme is demonstrated for high bandgap perovskites. This concurrent bulk-passivation and surface-passivation scheme is based on the partial diffusion of bulky organic cations from the surface-layer into the bulk passivating defects while the surface-remaining cations passivate the perovskite surface. This is similar to the previous work by Mahmud et al.[10] except this time the bulky organic cations are responsible for both bulk and surface passivations while previous work relied on the diffused-halide from the surface to passivate the perovskite bulk.

The partial diffusion of organic bulky cations into the bulk is possible if their ionic radii are comparable to the organic cations in the perovskite bulk. This is otherwise not possible with larger cations.[11] Evidence of the cation diffusion is seen in ionic distribution profiling, Fourier transform infrared spectroscopy, and crystallography and one of its effect on the perovskite device is bandgap widening.

More importantly, performance of high-bandgap (1.75 eV) champion p–i–n perovskite solar cell devices improved by 1% absolute after implementing the concurrent bulk and surface passivation scheme on one side and another 1% absolute if implemented on both sides. The champion cell achieved the highest FF of 86.5% and power conversion efficiency of 20.2%. These values are the highest for perovskite cells with bandgap >1.7 eV (Figure S1, Supporting Information). The new knowledge on cation diffusion generated from this work will inspire new approaches for simultaneous bulk and interface passivations of perovskite films for future devices, especially those with high bandgaps for tandem applications.

2. Results and Discussion

For the cation-diffusion-passivation-scheme, we have chosen $CH_6N_3^+$ (guanidinium, abbreviated as Gu),[6g] which has an ionic radius (0.278 nm for Gu^+) comparable to that (0.253 nm)[12] of formamidinium ($HC(NH_2)_2$), abbreviated as FA). For high bandgap perovskite cell demonstration, p–i–n device structure using SAM-based HTL ([2-(3,6-dimethoxy-9H-carbazol-9-yl) ethyl]phosphonic acid (MeO-2PACz)) as shown in **Figure 1**a was used. Details of device fabrication can be found in the Supporting Information. The concentration of GuBr precursor was first optimized for the best double-sided (DS) passivations in terms of device performance (Figure S2, Supporting Information). A concentration of 2 mg mL^{-1} was found to be the optimum and was used in subsequent experiments.

For physical characterization of the cell structure, scanning electron microscopy (SEM) cross-sectional imaging was first used. While the relatively thick indium tin oxide (ITO), perovskite and Cu layers can be easily distinguished as shown in Figure S3 of the Supporting Information, the ultrathin Gu^+ cation-based passivation layer, HTL, and ETL stack consisting of BCP/C60/LiF cannot be easily seen under the SEM for any of the control, single-sided (SS) or DS passivated cells. We therefore conducted transmission electron microscopy energy-dispersive X-ray spectroscopy (TEM-EDX) cross-sectional imaging to identify such ultrathin layer. Figure 1b shows the TEM cross sectional image of the perovskite photoabsorber layer and the perovskite/ETL interface and the corresponding EDX mappings in Figure 1c–j. From the individual EDX elemental maps we can observe Cu-rich Cu layer (Figure 1c), C-rich C_{60} layer (Figure 1d) and F-rich LiF layer (Figure 1e). Figure 1g–j shows the perovskite photoabsorbing layer rich in I (Figure 1g), Pb (Figure 1h), and Cs (Figure 1j). Just on top of this layer is a N-rich (Figure 1f) and Br-rich (Figure 1g) layer. From the X-ray photoelectron spectroscopy (XPS) surface elemental analysis (**Figure 2**), we confirmed that this N- and Br-rich layer is the GuBr (CH_6N_3Br) passivation layer, which significantly increases N (by ≈37%) and Br (by ≈40%) contents at the control perovskite surface (Table S1, Supporting Information). We note that the passivation layer (≈10 nm) had some overlap with the LiF inorganic layer indicating nonuniform and discontinuity of these films hinting possible diffusion of

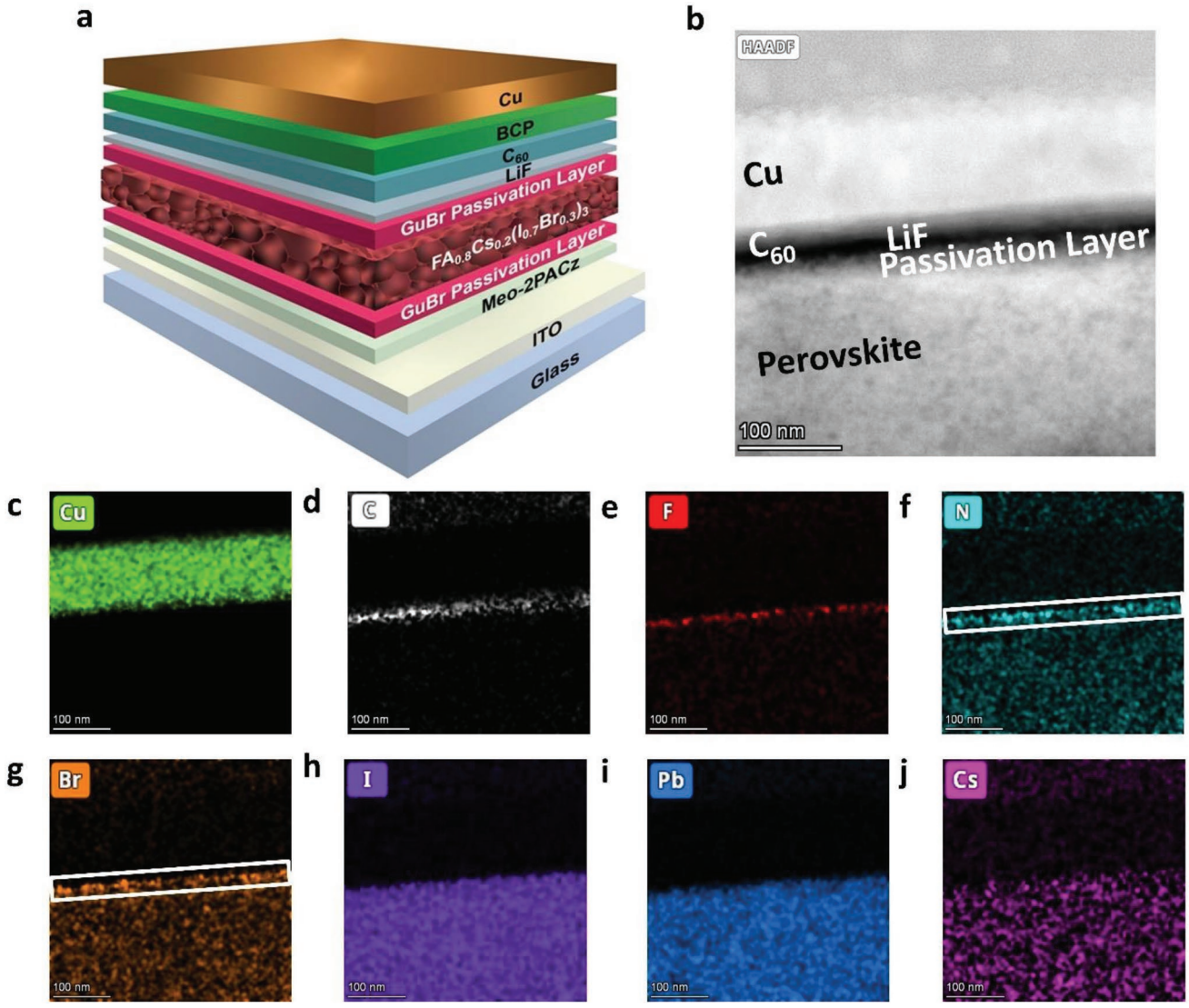

Figure 1. a) Schematic diagram showing the cell structure for high bandgap p–i–n perovskite solar cell demonstration using SAM-based HTL and double-sided (DS) passivation layers sandwiching the bulk perovskite film. b) Transmission electron microscopy (TEM) cross-sectional image and respective energy-dispersive X-ray spectroscopy (EDX) elemental mapping of c) copper, d) carbon, e) fluorine, f) nitrogen, g) bromine, h) iodine, i) lead, and j) cesium for the perovskite layer and the perovskite/ETL interface. The rectangular box in (f) and (g) mark the top passivation layer which is N- and Br-rich.

some of passivation materials into the perovskite bulk due to the partial dissolution of perovskite film[7b] in the highly polar precursor solution (2-propanol based) of Gu^+ cation. We also attempted similar characterizations of the passivation layer at the perovskite/HTL interface (Figure S4, Supporting Information). It was harder to identify the GuBr under TEM imaging in this case as the organic materials in the GuBr passivation layer and MeO-2PACz HTL under the perovskite film are very sensitive to the electron beam during the lamella preparation for TEM cross-section and the bottom interface cracked very fast even before the lamella is thinned down to 100 nm (Figure S4, Supporting Information). Therefore, we used XPS characterization to confirm the presence of the passivation layer underneath the perovskite film. However, prior to that, to mimic the solvent exposure that the GuBr passivation layer would have experienced in full device fabrication, the GuBr layer was exposed to the DMF/NMP solvent mixture (where DMF = *N*,*N*-dimethylformamide and NMP = *N*-methyl-2-pyrrolidone) prior to XPS surface elemental analysis. Results still showed the presence of Br^- anions on the surface (Figure S5, Supporting Information) indicating successful deposition of the GuBr passivation layer on the MeO-2PACz ($C_{16}H_{18}NO_5P$) layer despite solvent exposure necessary for full device fabrication.

Given the knowledge of the stronger presence of GuBr at the perovskite/ETL interface (the "rear" side of the perovskite photoabsorber with respect to illumination) compared to the perovskite/HTL interface (the "front" side), we confirmed such effect on device performance by comparing rear-sided-passivated and front-sided-passivated cells. Results are shown in Figure S6 of the Supporting Information. It is clear that cells

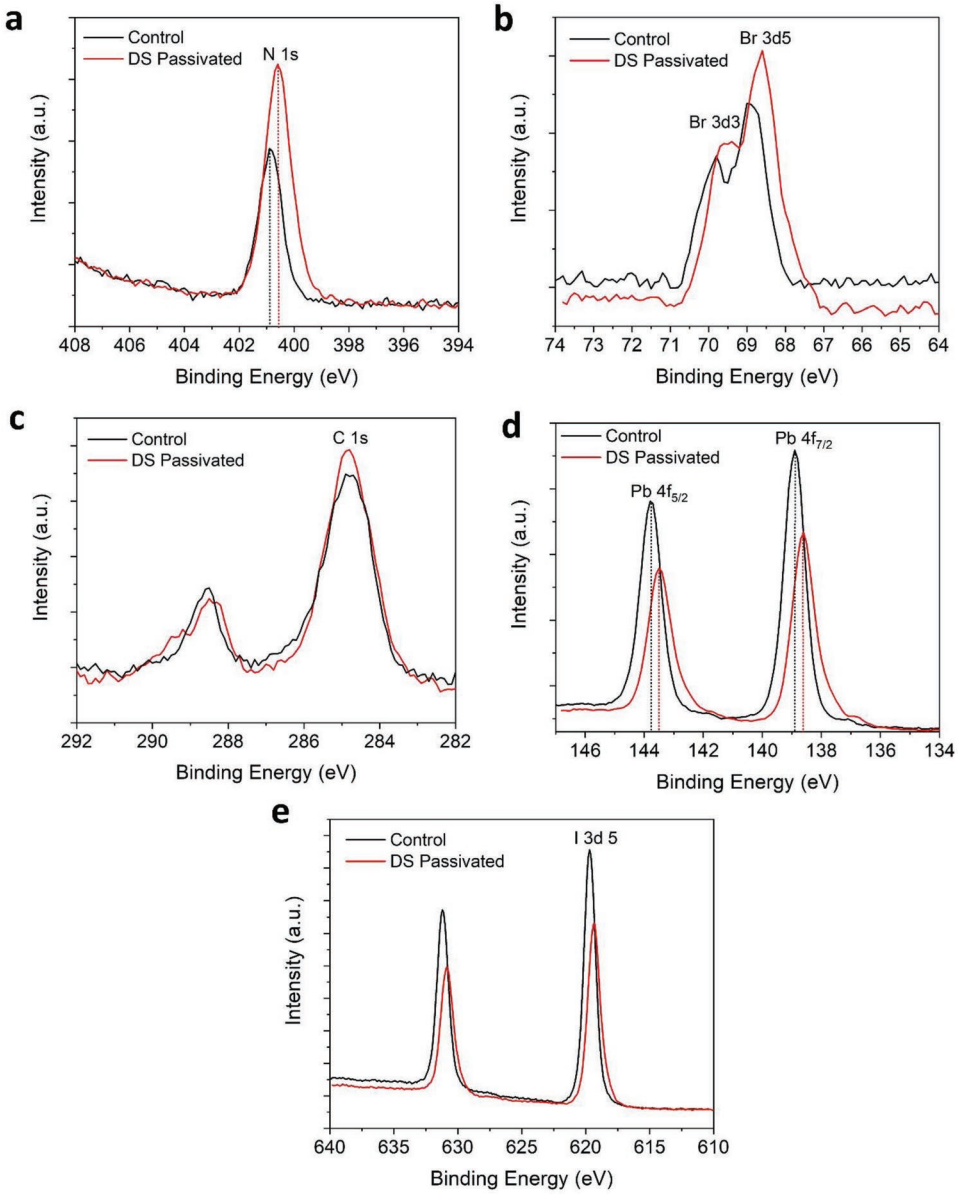

Figure 2. High resolution X-ray photoelectron spectroscopy (XPS) spectra of a) N 1s, b) Br 3d, c) C1s, d) Pb 4f, and e) I 3d of the surface of unpassivated (control) and DS passivated perovskite films.

with rear passivation (stronger presence of GuBr) show better performance than those with front passivation from improved open-circuit voltage (V_{OC}). Therefore, for subsequent comparisons between SS and DS passivation, rear passivation will be used for the SS passivation case. Results in **Figure 3**a and **Table 1** show that average performance improvement by more than 1% absolute from SS passivation was already quite significant due to the ≈100 mV increase in average V_{OC}. DS passivation provided a smaller average V_{OC} improvement (≈30 mV) but the major impact was the higher average FF produced, by 1% absolute thereby delivering another 1% absolute average efficiency improvement. In addition, minimum hysteresis was observed in the demonstrated devices in this work (Figure S7 and Table S2, Supporting Information). To the best of our knowledge, both the FF and PCE values of the champion DS passivated cell are the highest for high bandgap (≥1.7 eV) perovskite cells reported (Figure S1, Supporting Information). While the very high FFs demonstrated by the DS passivated cells were a result of reduced parasitic resistances (reduction of series resistance and increase of shunt resistance as the application of passivation layers increased), it was also due to other effects that warranted further investigations as reported below.

To further understand the effect of DS passivation on material properties and device performance, we first investigated the surface morphology and topology of the perovskite film with and without passivations via top-view SEM and atomic force microscopy (AFM). Both SS and DS passivations involve the deposition of an ultrathin GuBr layer on top of the perovskite. However, they did not appear to affect the grain size of

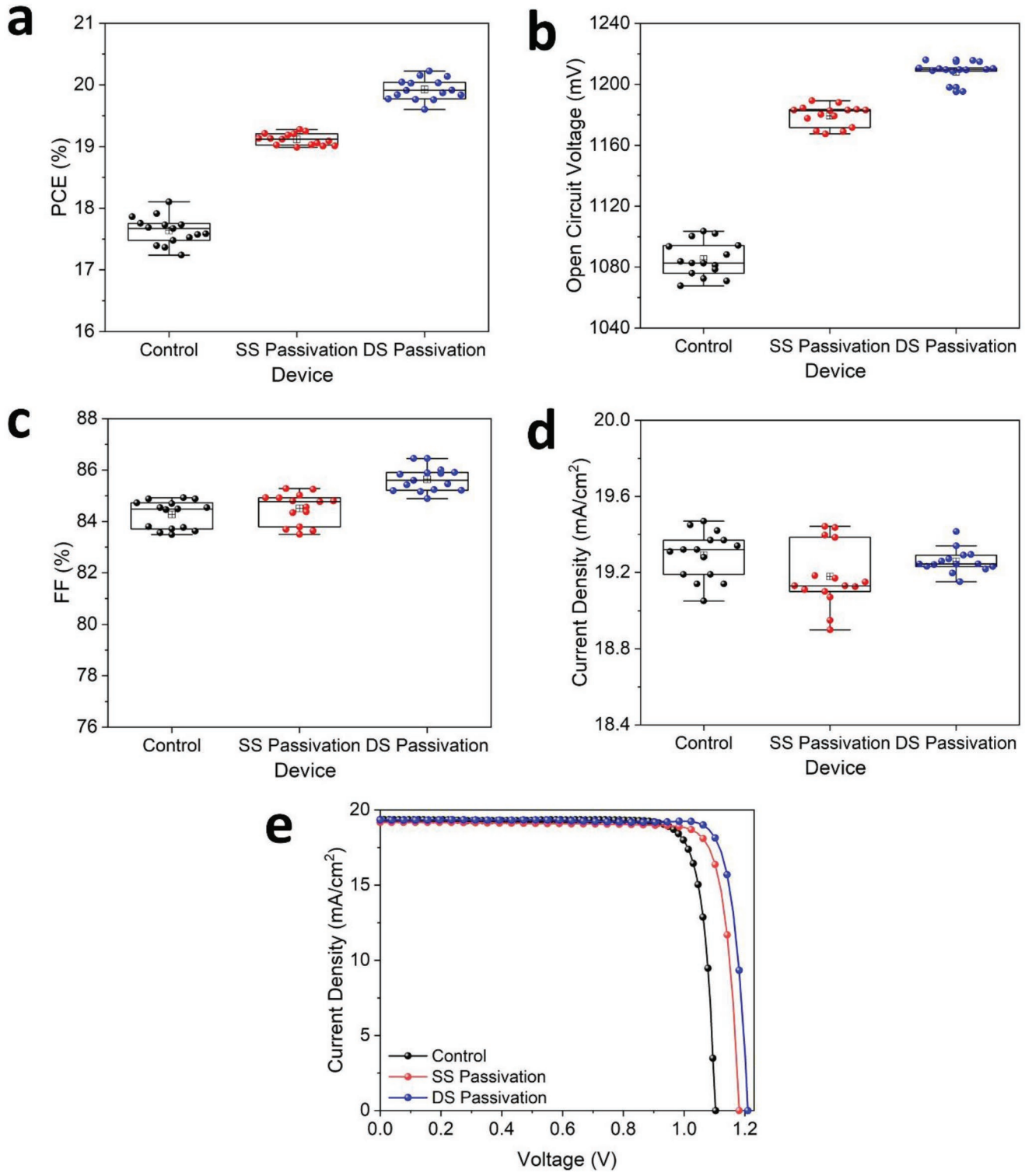

Figure 3. Statistical distribution of photovoltaic parameters in *J–V* characterization: a) distribution of PCE, b) distribution of V_{OC}, c) distribution of FF, and d) distribution of current density J_{SC} (the data are based on the *J–V* results from 15 cells of each kind of device) and e) *J–V* curves of the champion control, SS passivation, and DS passivation cells (reverse scan).

the perovskite films as seen in Figure S8 of the Supporting Information. The ultrathin passivation layers did not significantly change the surface topology of the perovskite films either with only a very small degree of film smoothing as a result of double-sided-passivation as measured by the AFM (Figure S9, Supporting Information).

Table 1. Photovoltaic parameters—averaged from 15 cells and measured for the champion device in each category: control (unpassivated), SS passivated, and DS passivated perovskite solar cells.

Device	Average/champion	V_{OC} [mV]	J_{SC} [mA cm^{-2}]	FF [%]	PCE [%]	Series resistance [Ω cm^2]	Shunt resistance [Ω cm^2]
Control	Average	1085 ± 11	19.3 ± 0.1	84.3 ± 0.5	17.6 ± 0.2	1.42 ± 0.16	3009 ± 1216
	Champion	1104	19.4	84.7	18.1	1.46	4563
SS passivation	Average	1179 ± 7	19.2 ± 0.2	84.5 ± 0.6	19.1 ± 0.1	1.34 ± 0.08	3108 ± 818
	Champion	1187	19.2	85.0	19.3	1.33	4602
DS passivation	Average	1208 ± 7	19.3 ± 0.1	85.6 ± 0.5	19.9 ± 0.2	1.04 ± 0.24	3335 ± 1420
	Champion	1210	19.3	86.5	20.2	1.15	5445

With regards to crystallinity of the perovskite films with and without passivations, results of X-ray diffraction (XRD) measurements in **Figure 4**a,b reveal the disappearance of PbI_2 peaks after SS and DS passivations. XPS analyses of the same samples also showed the reduction of Pb and I signals after passivations (Figure 2d–e). This is likely to be due to the reaction between GuBr and PbI_2 that is otherwise present on the surface of control (unpassivated) perovskite film. This phenomenon is not uncommon in perovskites employing surface passivating layer.[13] We then took a closer look at the (110) diffraction peak of control and passivated films in the XRD pattern (Figure 4b) which shifted to lower angles by 0.1° and 0.04°, respectively for DS and SS passivated films compared to the control suggesting unit cell volume expansion.[14] This suggests diffusion of Gu^+ which has a slightly larger ionic radius than FA^+.[12]

To confirm the existence of Gu^+ cation in the perovskite bulk, we conducted Fourier transform infrared spectroscopy on control and passivated films. Results in Figure 4c,d show the existence of the characteristic perovskite peaks[15] (Figure 4c) as well as an additional peak in the passivated films at 1650 cm^{-1} corresponding to the asymmetric vibration of C–N group in Gu^+ cation.[16]

Gu^+ diffusion from the passivation layer into the perovskite bulk was also confirmed by ionic distribution profiling of the fabricated cells using time-of-flight secondary ion mass spectrometry (ToF-SIMS). Results in Figure 4e–g show that Gu^+ ($CH_6N_3^+$) species cannot be found in control devices (Figure 4e) but can be found on the surfaces and within the perovskite bulk in both SS and DS passivated cells (green curve in Figure 4f–g). The diffusion of Gu^+ cation is more pronounced in DS passivated cells (well above the 50% normalized intensity line) as expected. This is because SS passivated cells only have one surface passivating layer (at the rear) rather than two layers as the source of Gu^+. This trend is also consistent with that of the XRD result showing larger unit cell volume expansion in DS passivated film. Results from ToF-SIMS also confirm that no Br^- diffusion from the passivating layers into the perovskite bulk could be observed (Figure S10, Supporting Information).

Now that we understand the effect of DS passivation on material properties, we look at the implications on optoelectronic properties and device performance. Results from i) external quantum efficiency (EQE) (**Figure 5**a), ii) optical absorbance (Figure 5b), and iii) steady-state photoluminescence (PL) measurements (Figure 5c) showed a small blue-shift or an increase (≈0.01 eV) in bandgap for SS and DS passivated films compared to the control. This is due to Gu^+ diffusion into the perovskite bulk. To simulate the effect of the presence of Gu^+ in the perovskite bulk, "bulk-passivated" perovskite films were fabricated whereby GuBr is mixed into the perovskite precursor for film fabrication. It was found that bandgap widening could also be observed in these samples by EQE measurement (Figure S11, Supporting Information). While the small bandgap increase can contribute to an increased V_{OC}, this effect alone would not be responsible for the significant V_{OC} enhancement (9% for SS, and 11% for DS from the baseline average V_{OC}) in passivated cells demonstrated (Table 1). It is clear from the measured steady-state PL (Figure 5c), time-resolved PL (TRPL) (Figure 5d), and PL imaging (Figure 5e–g) that quality of the perovskite films improves with passivations. The increase in PL intensity (Figure 5c,e–g, Supporting Information) and increase in effective lifetime (Table S3, Supporting Information) of passivated perovskite films correlate with the increase in V_{OC}'s of passivated cells.

Light intensity-dependent V_{OC} measurement (**Figure 6**a) and temperature-dependent V_{OC} measurement (Figure 6c) allow for the determination of ideality factor (n) and activation energy (E_a) of recombination current. More details of the calculations can be found in the Supporting Information. Results from Figure 6a show that passivation reduces ideality factor from 1.73 for control cells to 1.19 for SS passivated cells and to 1.08 (close to 1) for DS passivated cells indicating suppression of trap-assisted Shockley–Read–Hall recombination.[17] To confirm this, thermal admittance spectroscopy (TAS) [18] was carried out to measure the density of shallow trap-states with and without passivation. Results are shown in Figure 6b where the x-axis represents the energy of trap-states with respect to the valence band. SS passivation reduced the density of trap-states by two orders of magnitude for Et_1 and Et_2 and an order for Et_3 and Et_4 compared to control cell. Their densities were further reduced by DS passivation. TAS was also carried out on "bulk-passivated" only cells (Figure S12, Supporting Information). Results show that Et_1 and Et_2 correspond to shallow bulk defects while Et_3 and Et_4 correspond to relatively deeper surface defects. This demonstrates the dual roles played by the GuBr passivation scheme explaining the significant improvements of V_{OC} and FF. Nevertheless, surface passivation is a more dominant role as evident by the results of temperature-dependent V_{OC} measurement (Figure 6c). Activation-energy (E_a) of recombination current increases with SS and DS passivations indicating the dominant recombination mechanism changed from surface to bulk[17b,18a,19] with passivations as they improve the quality of the surface(s).

As part of the supplementary work, built-in-potentials (V_{bi}) of the controls and passivated cells were also determined from

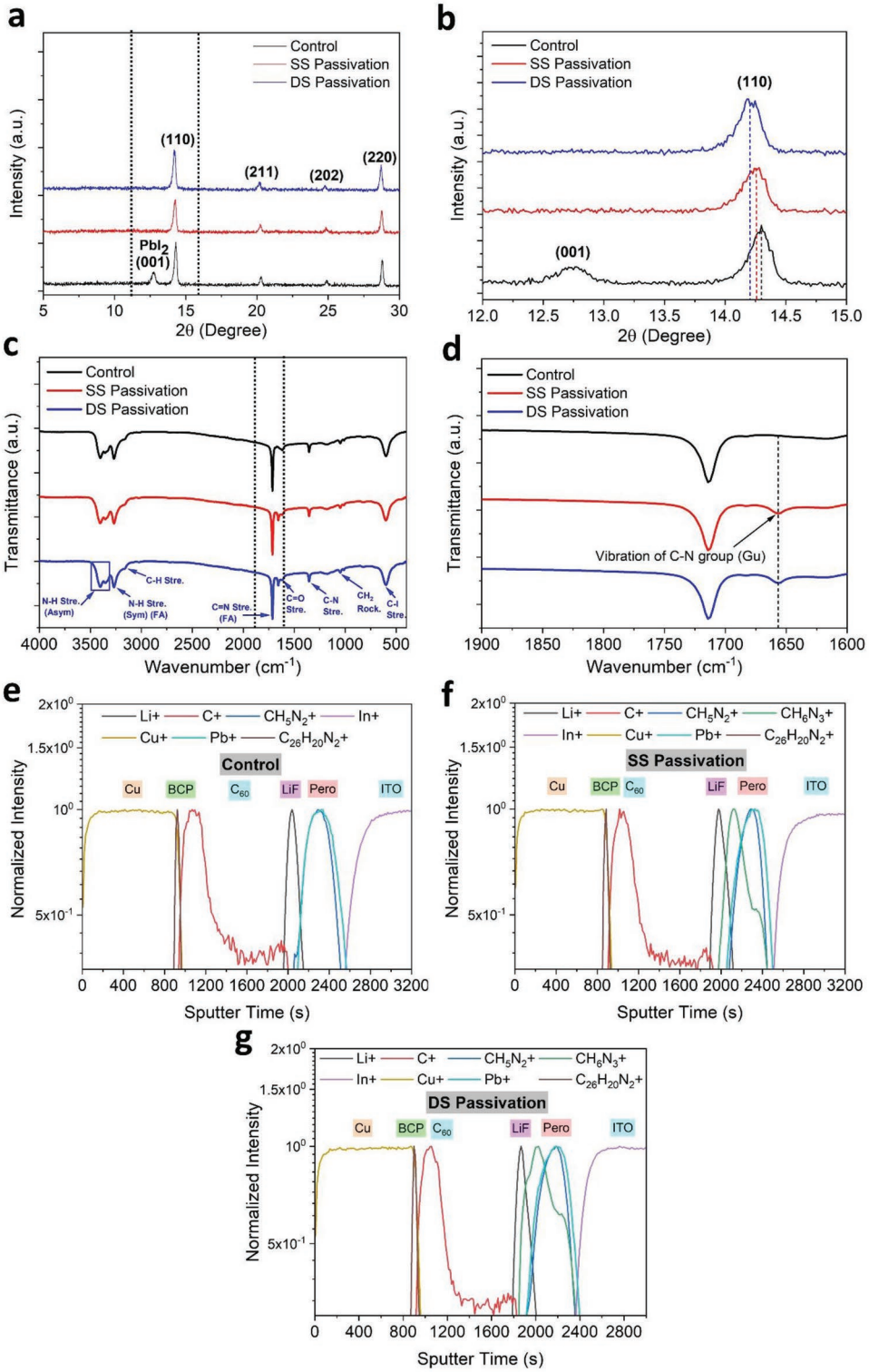

Figure 4. a) X-ray diffraction (XRD) patterns of control, SS and DS passivated perovskite films, b) zooming in to the (110) diffraction peak. c) Fourier transform infrared spectroscopy (FTIR) spectra of control and passivated films, d) zooming in to the wavenumber region 1900–1600 cm^{-1} showing the additional the C–N vibration peak in passivated films. Time-of-flight secondary ion mass spectrometry (ToF-SIMS) of e) control, f) SS, and g) DS passivated devices.

Mott–Schottky analysis (Figure S13a, Supporting Information). The trend correlates with that of the V_{OC}'s. We can conclude that the V_{bi} improvement is solely from bulk and surface passivations suppressing trap-assisted recombination and not from changes in the energy band alignment caused by the insertion of the interface passivation layer. This is confirmed by XPS and ultraviolet

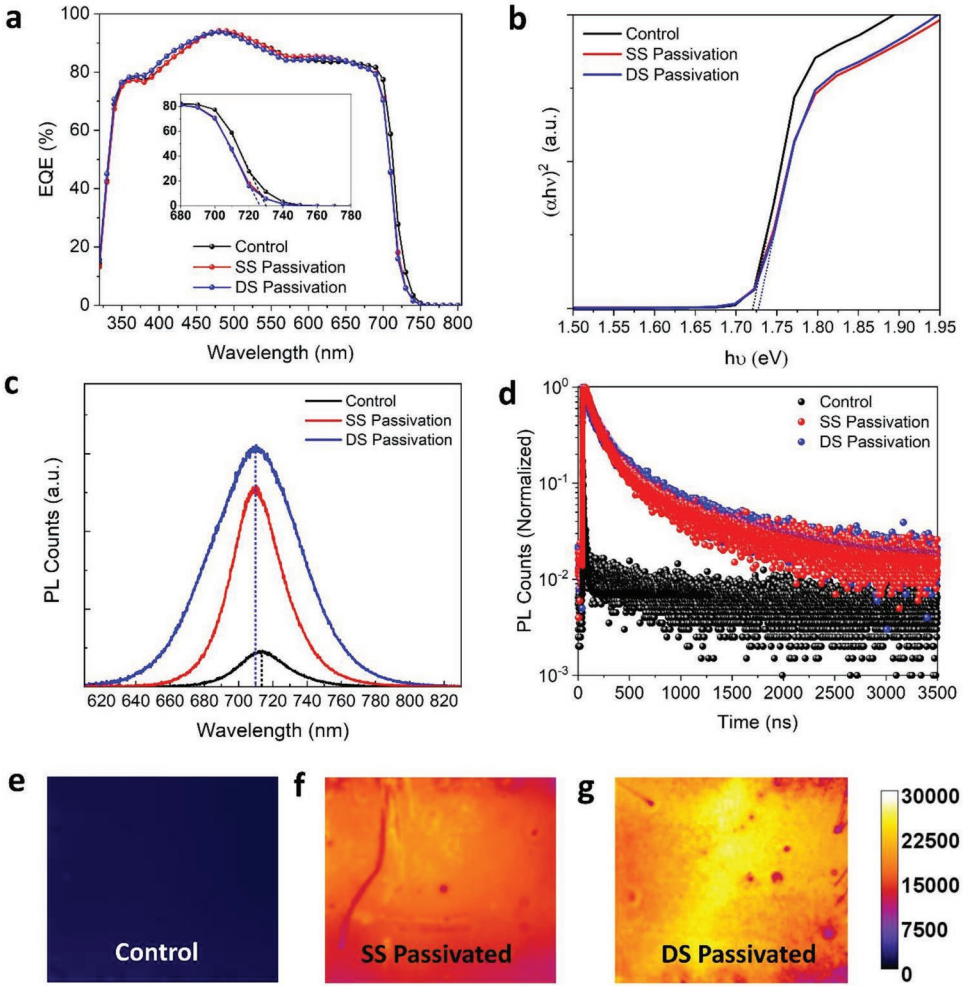

Figure 5. a) External quantum efficiency (EQE) curves, b) Tauc plots of control (unpassivated), SS and DS passivated cells. The inset in (a) shows bandgap widening in the SS and DS passivated cell compared to the controls. c) Steady-state photoluminescence (PL) spectra, d) experimental and fitted time-resolved photoluminescence (TRPL) curves, and e–g) PL imaging of control (unpassivated), SS and DS and passivated perovskite films on MeO-2PACz/ITO/glass substrates.

photoelectron spectroscopy showing no changes in the valence band maxima (Figure S13b, Supporting Information) or work function position (Figure S13c, Supporting Information) of the passivated film. The respectable current output and outstanding fill factor of our cells show that the absorber layer thickness, bulk and surface passivations have been optimized well with parasitic resistances minimized. For future work, development of carrier transport or selective layers with better energy band alignments will further improve the voltage output of these cells. Part of future work can be the exploration of other passivators with organic components like azetidinium $[(CH_2)_3NH_2]^+$,[20] which has similar ionic radii (0.25 nm) as those of the typical cations used in high performing perovskites for solar cell applications.

Finally we present preliminary stability data of encapsulated (based on poly-isobutylene polymer "blanket" approach)[21] cells in Figure S14 of the Supporting Information, which exhibited negligible efficiency drop after 1000 h of storage in the dark at 20–25 °C and 20–30% relative humidity. Further work will be conducted to examine their light and thermal stabilities which are important for applications in tandem solar cells.

3. Conclusion

In summary, we report a cation-diffusion-based double-sided interface passivation scheme for a high bandgap perovskite cell which also provides bulk passivation at the same time and is compatible with a p–i–n cell architecture. Record FF (86.5%) and PCE (20.2%) are achieved by our champion 1.75 eV perovskite solar cell. We report the evidence of partial cation diffusion from the Gu-based passivation layers into the perovskite bulk and its benefit which is the suppression the shallow traps in the bulk. The remaining Gu cations at the perovskite/ETL and perovskite/HTL interfaces are responsible for passivating the relatively deeper surface trap-states. The end result of concurrent bulk and surface passivations based on cation diffusion was the demonstration of record FF and PCE for high bandgap perovskite solar cell. This opens up new avenues for future passivation schemes based on ionic diffusion which can be extended to functionalized and tailored passivation molecules for further efficiency enhancement for single-junction and tandem perovskite solar cells.

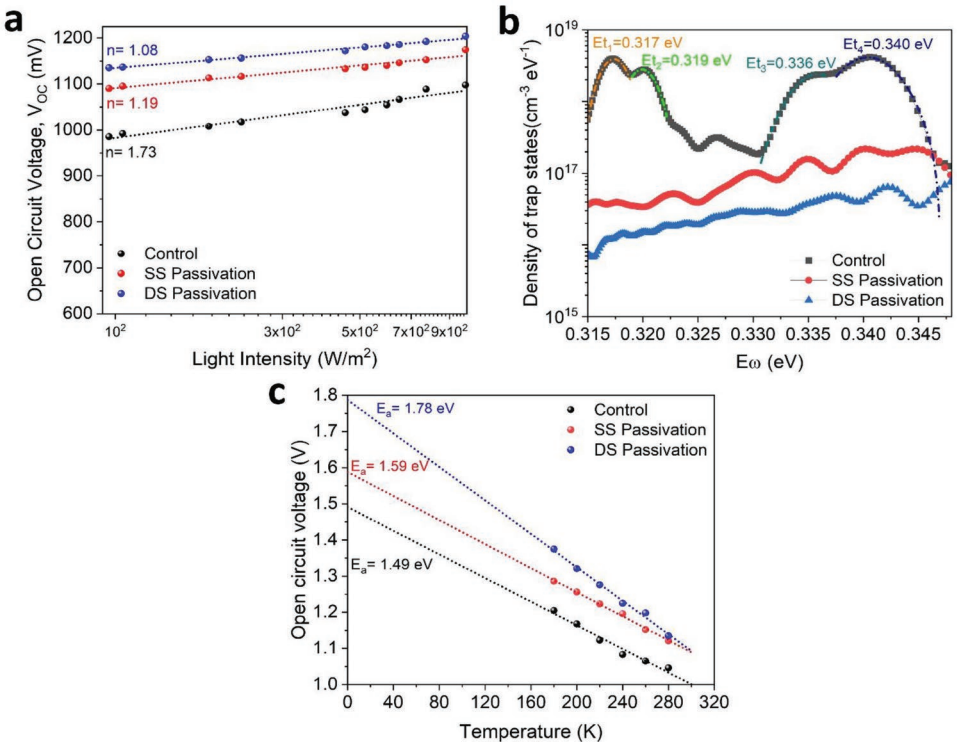

Figure 6. a) Light intensity-dependent V_{OC} plot showing the ideality factors (n) determined from the slopes of the fitted lines, b) thermal admittance spectroscopy (TAS) showing the density of defect states with energy with respect to valence band, and c) temperature-dependent V_{OC} plot showing the activation-energies (E_a) of recombination currents (y-axis intercept at 0 K) of control, SS and DS, and passivated cells.

4. Experimental Section

Experimental details are provided in the Supporting Information.

Supporting Information

Supporting Information is available from the Wiley Online Library or from the author.

Acknowledgements

M.A.M. and J.Z. contributed equally to this work. The authors acknowledge the facilities and the scientific and technical assistance of Sydney Analytical, a core research facility at The University of Sydney. The authors also acknowledge the technical and scientific assistance provided by i) Research & Prototype Foundry Core Research Facility at the University of Sydney, part of the Australian National Fabrication Facility, ii) Sydney Microscopy & Microanalysis, the University of Sydney node of Microscopy Australia, iii) Electron Microscopy Unit at University of New South Wales (UNSW), and iv) Surface Analysis Laboratory, Solid State & Elemental Analysis Unit at Mark Wainwright Analytical Centre at UNSW. This work was supported by the Australian Government through the Australian Renewable Energy Agency (ARENA) via projects 2020 RND001 and 2020 RND003. S.T. and C.L. acknowledge the support of the John Hooke Chair of Nanoscience Postgraduate Research Scholarships. J.C. and A.W.Y.H.-B. were supported by the Australian Research Council (ARC) Future Fellowships FT210100210 and FT180100232, respectively.

Open access publishing facilitated by The University of Sydney, as part of the Wiley - The University of Sydney agreement via the Council of Australian University Librarians.

Conflict of Interest

The authors declare no conflict of interest.

Data Availability Statement

The data that support the findings of this study are available from the corresponding author upon reasonable request.

Keywords

bulk passivation, cation diffusion, high bandgap perovskites, surface passivation

Received: May 15, 2022
Revised: June 29, 2022
Published online: August 2, 2022

[1] A. S. Subbiah, F. H. Isikgor, C. T. Howells, M. De Bastiani, J. Liu, E. Aydin, F. Furlan, T. G. Allen, F. Xu, S. Zhumagali, S. Hoogland, E. H. Sargent, I. McCulloch, S. De Wolf, *ACS Energy Lett.* **2020**, *5*, 3034.
[2] A. W. Y. Ho-Baillie, J. Zheng, M. A. Mahmud, F.-J. Ma, D. R. McKenzie, M. A. Green, **2021**, *8*, 041307.
[3] M. A. Green, A. W. Y. Ho-Baillie, *ACS Energy Lett.* **2019**, *4*, 1639.
[4] S. Mahesh, J. M. Ball, R. D. J. Oliver, D. P. McMeekin, P. K. Nayak, M. B. Johnston, H. J. Snaith, *Energy Environ. Sci.* **2020**, *13*, 258.

[5] a) Y. Zhou, Y.-H. Jia, H.-H. Fang, M. A. Loi, F.-Y. Xie, L. Gong, M.-C. Qin, X.-H. Lu, C.-P. Wong, N. Zhao, **2018**, *28*, 1803130; b) F. Jiang, D. Yang, Y. Jiang, T. Liu, X. Zhao, Y. Ming, B. Luo, F. Qin, J. Fan, H. Han, L. Zhang, Y. Zhou, *J. Am. Chem. Soc.* **2018**, *140*, 1019; c) J. Zhang, Z. Wang, A. Mishra, M. Yu, M. Shasti, W. Tress, D. J. Kubicki, C. E. Avalos, H. Lu, Y. Liu, B. I. Carlsen, A. Agarwalla, Z. Wang, W. Xiang, L. Emsley, Z. Zhang, M. Grätzel, W. Guo, A. Hagfeldt, *Joule* **2020**, *4*, 222; d) W. Xiang, Z. Wang, D. J. Kubicki, W. Tress, J. Luo, D. Prochowicz, S. Akin, L. Emsley, J. Zhou, G. Dietler, M. Grätzel, A. Hagfeldt, *Joule* **2019**, *3*, 205; e) H. Zhao, Y. Han, Z. Xu, C. Duan, S. Yang, S. Yuan, Z. Yang, Z. Liu, S. Liu, *Adv. Energy Mater.* **2019**, *9*, 1902279; f) S. Yang, H. Zhao, Y. Han, C. Duan, Z. Liu, S. Liu, *Small* **2019**, *15*, 1904387.

[6] a) L. Wang, Z. Yan, J. Qiu, J. Wu, C. Zhen, K. Tai, X. Jiang, S. Yang, *Nano Energy* **2021**, *90*, 106537; b) T. Duong, H. Pham, Y. Yin, J. Peng, M. A. Mahmud, Y. Wu, H. Shen, J. Zheng, T. Tran-Phu, T. Lu, L. Li, A. Kumar, G. G. Andersson, A. W. Y. Ho-Baillie, Y. Liu, T. White, K. Weber, K. Catchpole, *J. Mater. Chem. A* **2021**, *9*, 18454; c) S. Gharibzadeh, P. Fassl, I. M. Hossain, P. Rohrbeck, M. Frericks, M. Schmidt, T. Duong, M. R. Khan, T. Abzieher, B. A. Nejand, F. Schackmar, O. Almora, T. Feeney, R. Singh, D. Fuchs, U. Lemmer, J. P. Hofmann, S. A. L. Weber, U. W. Paetzold, *Energy Environ. Sci.* **2021**, *14*, 5875; d) T. Duong, H. Pham, T. C. Kho, P. Phang, K. C. Fong, D. Yan, Y. Yin, J. Peng, M. A. Mahmud, S. Gharibzadeh, B. A. Nejand, I. M. Hossain, M. R. Khan, N. Mozaffari, Y. Wu, H. Shen, J. Zheng, H. Mai, W. Liang, C. Samundsett, M. Stocks, K. McIntosh, G. G. Andersson, U. Lemmer, B. S. Richards, U. W. Paetzold, A. Ho-Ballie, Y. Liu, D. Macdonald, A. Blakers, et al., *Adv. Energy Mater.* **2020**, *10*, 1903553; e) S. Gharibzadeh, B. Abdollahi Nejand, M. Jakoby, T. Abzieher, D. Hauschild, S. Moghadamzadeh, J. A. Schwenzer, P. Brenner, R. Schmager, A. A. Haghighirad, L. Weinhardt, U. Lemmer, B. S. Richards, I. A. Howard, U. W. Paetzold, *Adv. Energy Mater.* **2019**, *9*, 1803699; f) Q. Ye, Y. Zhao, S. Mu, F. Ma, F. Gao, Z. Chu, Z. Yin, P. Gao, X. Zhang, J. You, *Adv. Mater.* **2019**, *31*, 1905143; g) C. Chen, Z. Song, C. Xiao, D. Zhao, N. Shrestha, C. Li, G. Yang, F. Yao, X. Zheng, R. J. Ellingson, C.-S. Jiang, M. Al-Jassim, K. Zhu, G. Fang, Y. Yan, *Nano Energy* **2019**, *61*, 141.

[7] a) J. Peng, J. I. Khan, W. Liu, E. Ugur, T. Duong, Y. Wu, H. Shen, K. Wang, H. Dang, E. Aydin, X. Yang, Y. Wan, K. J. Weber, K. R. Catchpole, F. Laquai, S. De Wolf, T. P. White, *Adv. Energy Mater.* **2018**, *8*, 1801208; b) M. A. Mahmud, T. Duong, Y. Yin, H. T. Pham, D. Walter, J. Peng, Y. Wu, L. Li, H. Shen, N. Wu, N. Mozaffari, G. Andersson, K. R. Catchpole, K. J. Weber, T. P. White, *Adv. Funct. Mater.* **2020**, *30*, 1907962; c) M. A. Mahmud, T. Duong, Y. Yin, J. Peng, Y. Wu, T. Lu, H. T. Pham, H. Shen, D. Walter, H. T. Nguyen, N. Mozaffari, G. D. Tabi, Y. Liu, G. Andersson, K. R. Catchpole, K. J. Weber, T. P. White, *Small* **2020**, *16*, 2005022; d) Y. Zhao, Q. Li, W. Zhou, Y. Hou, Y. Zhao, R. Fu, D. Yu, X. Liu, Q. Zhao, **2019**, *3*, 1800296.

[8] A. Al-Ashouri, E. Köhnen, B. Li, A. Magomedov, H. Hempel, P. Caprioglio, J. A. Márquez, A. B. M. Vilches, E. Kasparavicius, J. A. Smith, N. Phung, D. Menzel, M. Grischek, L. Kegelmann, D. Skroblin, C. Gollwitzer, T. Malinauskas, M. Jošt, G. Matič, B. Rech, R. Schlatmann, M. Topič, L. Korte, A. Abate, B. Stannowski, D. Neher, M. Stolterfoht, T. Unold, V. Getautis, S. Albrecht, *Science* **2020**, *370*, 1300.

[9] M. Degani, Q. An, M. Albaladejo-Siguan, Y. J. Hofstetter, C. Cho, F. Paulus, G. Grancini, Y. Vaynzof, *Sci. Adv.* **2021**, *7*, 7930.

[10] M. A. Mahmud, H. T. Pham, T. Duong, Y. Yin, J. Peng, Y. Wu, W. Liang, L. Li, A. Kumar, H. Shen, D. Walter, H. T. Nguyen, N. Mozaffari, G. D. Tabi, G. Andersson, K. R. Catchpole, K. J. Weber, T. P. White, *Adv. Funct. Mater.* **2021**, *31*, 2104251.

[11] Z. Huang, A. H. Proppe, H. Tan, M. I. Saidaminov, F. Tan, A. Mei, C.-S. Tan, M. Wei, Y. Hou, H. Han, S. O. Kelley, E. H. Sargent, *ACS Energy Lett.* **2019**, *4*, 1521.

[12] W. Zhang, J. Xiong, J. Li, W. A. Daoud, *J. Mater. Chem. A* **2019**, *7*, 9486.

[13] Y. Cho, A. M. Soufiani, J. S. Yun, J. Kim, D. S. Lee, J. Seidel, X. Deng, M. A. Green, S. Huang, A. W. Y. Ho-Baillie, *Adv. Energy Mater.* **2018**, *8*, 1703392.

[14] J. Xu, C. C. Boyd, Z. J. Yu, A. F. Palmstrom, D. J. Witter, B. W. Larson, R. M. France, J. Werner, S. P. Harvey, E. J. Wolf, W. Weigand, S. Manzoor, M. F. A. M. van Hest, J. J. Berry, J. M. Luther, Z. C. Holman, M. D. McGehee, *Science* **2020**, *367*, 1097.

[15] a) M. Jung, T. J. Shin, J. Seo, G. Kim, S. I. Seok, *Energy Environ. Sci.* **2018**, *11*, 2188; b) M. Acik, T. M. Alam, F. Guo, Y. Ren, B. Lee, R. A. Rosenberg, J. F. Mitchell, I. K. Park, G. Lee, S. B. Darling, *Adv. Energy Mater.* **2018**, *8*, 1701726; c) X. Guo, C. McCleese, C. Kolodziej, A. C. S. Samia, Y. Zhao, C. Burda, *Dalton Trans.* **2016**, *45*, 3806.

[16] M. Daub, C. Haber, H. Hillebrecht, *Eur. J. Inorg. Chem.* **2017**, *2017*, 1120.

[17] a) D. Glowienka, Y. Galagan, *Adv. Mater.* **2022**, *34*, 2105920; b) Y. Cho, H. D. Kim, J. Zheng, J. Bing, Y. Li, M. Zhang, M. A. Green, A. Wakamiya, S. Huang, H. Ohkita, A. W. Y. Ho-Baillie, *ACS Energy Lett.* **2021**, *6*, 925; c) Y. Cho, J. Bing, H. D. Kim, Y. Li, J. Zheng, S. Tang, M. A. Green, A. Wakamiya, S. Huang, H. Ohkita, A. W. Y. Ho-Baillie, *ACS Appl. Mater. Interfaces* **2021**, *13*, 39178.

[18] a) S. Tang, J. Bing, J. Zheng, J. Tang, Y. Li, M. Mayyas, Y. Cho, T. W. Jones, T. C.-J. Yang, L. Yuan, M. Tebyetekerwa, H. T. Nguyen, M. P. Nielsen, N. J. Ekins-Daukes, K. Kalantar-Zadeh, G. J. Wilson, D. R. McKenzie, S. Huang, A. W. Y. Ho-Baillie, *Cell Rep. Phys. Sci.* **2021**, *2*, 100511; b) H.-S. Duan, H. Zhou, Q. Chen, P. Sun, S. Luo, T.-B. Song, B. Bob, Y. Yang, *Phys. Chem. Chem. Phys.* **2015**, *17*, 112.

[19] W. Tress, M. Yavari, K. Domanski, P. Yadav, B. Niesen, J. P. Correa Baena, A. Hagfeldt, M. Graetzel, *Energy Environ. Sci.* **2018**, *11*, 151.

[20] G. Kieslich, S. Sun, A. K. Cheetham, *Chem. Sci.* **2014**, *5*, 4712.

[21] L. Shi, M. P. Bucknall, T. L. Young, M. Zhang, L. Hu, J. Bing, D. S. Lee, J. Kim, T. Wu, N. Takamure, D. R. McKenzie, S. Huang, M. A. Green, A. W. Y. Ho-Baillie, *Science* **2020**, *368*, 2412.